

# Trajectory arclength reveals chaos

Javier Jiménez-López<sup>\*1</sup> and V. J. García-Garrido<sup>†2</sup>

<sup>1</sup>Departamento de Física Teórica, Universidad Complutense de Madrid,  
E-28040 Madrid, Spain

<sup>2</sup>Departamento de Física y Matemáticas, Facultad de Ciencias, Universidad  
de Alcalá, 28805 Alcalá de Henares, Madrid, Spain.

February 10, 2026

## Abstract

In this paper we demonstrate that the phase space arclength of a trajectory, quantified by the time-averaged Lagrangian descriptor, is a robust and self-contained chaos indicator. By invoking Birkhoff's Ergodic Partition Theorem, we show that this scalar function distinguishes dynamical regimes via its power spectral density: for regular motion it converges to a delta function, whereas for chaotic trajectories the spectrum exhibits an inverse power-law ( $1/\omega$ ) driven by the phenomenon of dynamical stickiness. With this approach, we avoid the computation and simulation of the variational equations and the usage of neighboring orbits, making it the simplest geometrical chaos indicator derivable from Lagrangian descriptors. Its computational efficiency enables the study of high-dimensional systems and allows the generation of large datasets of classified initial conditions, ideal for training Machine Learning models. We validate these findings using the Hénon-Heiles and the Fermi-Pasta-Ulam systems. By linking the geometrical properties of phase space to spectral analysis, this work provides the mathematical justification to establish Lagrangian descriptors as a rigorous, self-sufficient framework for the global analysis of chaos and regularity in Hamiltonian systems.

**keywords:** Phase space, Chaos indicators, Lagrangian descriptors, Hamiltonian dynamics, Dynamical systems.

## 1 Introduction

One of the central aims of dynamical systems theory is to understand how trajectories evolve over time. In particular, the distinction of predictable, structured regular motion from chaos is of great fundamental and practical interest. Gaining insight into these contrasting regimes is of the utmost importance. While regular dynamics allow for reliable forecasting, chaotic systems are inherently limited in their predictability as slight variations in the initial conditions can cause significant divergences in the long-term behavior. Far from being a mere mathematical artifact, chaos is a fundamental dynamical phenomenon present across a wide range of fields in physics, chemistry, engineering and computer science. From the macroscopic unpredictability of weather patterns [61] and the stability of planetary motion [50, 10], chaos plays a critical role in celestial mechanics, influencing the transport of navigation satellites [15, 16], spacecraft steering [31], the confinement of stars in barred galaxy models [67] and the motion of particles in the surroundings of black holes [59, 49, 60]. In the realm of high energy physics, beam dynamics in circular particle accelerators are governed by chaotic stability limits [45, 3, 41]. At the microscopic scale, chaos shapes chemical reaction manifolds [65], drives dynamics in semiconductor microcavities [11] and emerges in quantum systems

---

<sup>\*</sup>javierj09@ucm.es (Corresponding author)  
<sup>†</sup>vjose.garcia@uah.es

ranging from cavity QED [39], the study of QFT [57] and nuclear spectral signatures [9] to critical points in quantum phase transitions [32]. Furthermore, the accurate detection of these regimes has become pivotal for modern computational applications, including the training of symplectic Machine Learning models designed to replicate the highly complex dynamics of Hamiltonian systems [17, 4] or classifiers that can improve the performance in determining the nature of large ensembles of initial conditions [22].

The quantitative distinction between regular and chaotic motion in phase space is achieved through chaos indicators, which are functions designed to produce significantly distinct asymptotic behaviors for chaotic and regular trajectories. Conventionally, these chaos indicators fall into two categories: those that rely on the evolution of deviation vectors, typically requiring the integration of the variational equations, and those that only need information from the evolution of the trajectory itself. In the first category, one can find the Fast Lyapunov Indicator (FLI) [14, 13], the maximum Lyapunov Exponent (mLE) [52], the Relative Lyapunov Indicator (RLI) [47], the Smaller Alignment Index (SALI) [51, 53, 54] and its generalization, the Generalized Alignment Index (GALI) [55, 40]. It has been recently shown that the latter can be computed through the multi-particle method [35], where instead of analyzing the evolution of  $k$  deviation vectors to obtain  $\text{GALI}_k$ , it is possible to evolve  $k$  neighboring orbits. Although this approach avoids the need of deriving and integrating the variational equations, it can still be computationally expensive to calculate  $\text{GALI}_k$  as  $k$  increases. Conversely, the second category encompasses Laskar's frequency map analysis [25], which is able to identify chaotic dynamics by monitoring the diffusion of the fundamental frequencies of the motion over time, and the Birkhoff averages method [26, 27, 8], which distinguishes regular from chaotic dynamics based on the convergence properties of time-averaged observables along the orbit. A comprehensive review of these methods can be found in [56].

In recent years, a new set of chaos indicators based on the mathematical framework of Lagrangian descriptors (LDs) has been introduced [21, 66, 7, 6, 23]. This methodology circumvents the derivation and integration of the variational equations, which in some cases can be a highly non-trivial task [20]. As a trajectory-based methodology [34, 28], the computation of these indicators is achieved by adding one extra differential equation to the system's equations of motion. This considerably reduces both the mathematical and computational complexity of chaos detection. In the present paper, we show how the trajectory arclength, formulated through the Lagrangian descriptor, has the capability of revealing the dynamical behavior of a trajectory. This is done by invoking Birkhoff's Ergodic Partition Theorem [58, 38] and analyzing the spectral signatures of the averaged time-evolution of the LD. As only the integration of the trajectory itself is required (no neighbors or deviation vectors), this stands as the simplest geometrical method for chaos detection. With its simplicity and computational efficiency, it will make possible the in-depth study of high-dimensional systems, which has remained a significant computational challenge. Furthermore, the fact that the LD can correctly distinguish between regular and chaotic dynamics, makes the whole mathematical framework of Lagrangian descriptors self-contained and robust for the detailed analysis of chaos in dynamical systems.

The paper is organized as follows. In Sec. 2, we provide a brief overview of the method of Lagrangian descriptors and analyze the properties of the time-averaged arclength,  $\Omega$ , via its spectral features and Birkhoff's Ergodic Partition Theorem. In Sec. 3, we present the numerical results obtained by applying this indicator to quantify chaos in two benchmark Hamiltonian models: the Hénon-Heiles system and the Fermi-Pasta-Ulam lattice. Among the obtained results, the most relevant one is the scaling of  $\Omega$ , found to be linear with increasing dimensionality, making the classification a  $\mathcal{O}(N)$  algorithm, where  $N$  is the number of degrees of freedom of the system. Finally, Sec. 4 summarizes our conclusions and outlines potential future directions. For completeness, we have included an appendix, see App. A, where we briefly describe SALI and GALI methods, which are the ground truth chaos indicators we have used throughout this work to validate our results.

## 2 Methodology

In this section, we establish the mathematical framework underlying the proposed chaos detection method based on Lagrangian descriptors. We begin in Sec. 2.1 with a review of the theoretical foundations of Lagrangian descriptors for continuous Hamiltonian systems, focusing on their arclength-based definition. Building on this, Sec. 2.2 introduces the time-averaged Lagrangian descriptor, where we derive its asymptotic behavior for both regular and chaotic motion, and analyze its properties in the frequency domain.

### 2.1 Lagrangian descriptors

Originally developed as a mathematical framework to analyze transport and mixing processes in geophysical flows [33, 37], Lagrangian descriptors have emerged as a powerful, trajectory-based scalar diagnostic tool for revealing phase space structures in general dynamical systems [64]. In this work we will focus on applying this method in the context of continuous Hamiltonian systems, although this approach can be used similarly for discrete systems.

Consider a Hamiltonian system with  $N$  degrees of freedom,  $\mathbf{q} = (q_1, \dots, q_N) \in \mathbb{R}^N$ , and conjugate momenta  $\mathbf{p} = (p_1, \dots, p_N) \in \mathbb{R}^N$ , which is defined by a scalar function  $H(\mathbf{x})$  that is conserved along trajectories, and  $\mathbf{x} = (\mathbf{q}, \mathbf{p}) \in \mathbb{R}^{2N}$  represents the state vector in the phase space of the system. In this context, Hamilton's equations of motion are given by the following set of ordinary differential equations:

$$\dot{\mathbf{x}} = J \nabla H, \quad (1)$$

where:

$$J = \begin{pmatrix} \mathbb{O}_N & \mathbb{I}_N \\ -\mathbb{I}_N & \mathbb{O}_N \end{pmatrix}, \quad (2)$$

is known as the Poisson matrix. Here,  $\mathbb{O}_N$  and  $\mathbb{I}_N$  denote the zero matrix and the identity matrix of order  $N$ , respectively.

A Lagrangian descriptor is a scalar function  $\mathcal{L}(\mathbf{x}_0, t_0, \tau)$  that assigns a non-negative value to an initial condition  $\mathbf{x}_0$  at time  $t_0$  based on the accumulation of a non-negative, scalar quantity  $\mathcal{F}(\mathbf{x}, t)$  along the evolution of the trajectory in phase space over time. The total LD value is defined as the sum of the forward and backward time integrations:

$$\mathcal{L}(\mathbf{x}_0, t_0, \tau) = \mathcal{L}_f(\mathbf{x}_0, t_0, \tau) + \mathcal{L}_b(\mathbf{x}_0, t_0, \tau), \quad (3)$$

where the forward ( $\mathcal{L}_f$ ) and backward ( $\mathcal{L}_b$ ) components are given by:

$$\mathcal{L}_f(\mathbf{x}_0, t_0, \tau) = \int_{t_0}^{t_0+\tau} \mathcal{F}(\mathbf{x}(t; \mathbf{x}_0), t) dt, \quad \mathcal{L}_b(\mathbf{x}_0, t_0, \tau) = \int_{t_0-\tau}^{t_0} \mathcal{F}(\mathbf{x}(t; \mathbf{x}_0), t) dt. \quad (4)$$

The integrand  $\mathcal{F}$  used to define Lagrangian descriptors typically quantifies geometric or physical properties of trajectories. In this work, we adopt the arclength formulation, in which  $\mathcal{F}$  is given by the Euclidean norm (2-norm) of the vector field. Specifically,

$$\mathcal{F}(\mathbf{x}, t) = \|\dot{\mathbf{x}}\| = \|\nabla H(\mathbf{x}, t)\|,$$

so that the LD integrand corresponds to the magnitude of the velocity vector. With this choice, the LD measures the arclength of the trajectory in phase space generated by the initial condition  $\mathbf{x}_0$  over the time interval  $[t_0 - \tau, t_0 + \tau]$ . It is worth noting that the Lagrangian descriptor formalism extends naturally to discrete dynamical systems (maps), where the integral definition is replaced by a finite summation over iterations [30]. Since the geometric interpretation and diagnostic capabilities of LDs are essentially the same in both discrete and continuous settings, we restrict our formal analysis and discussion to the time-continuous case. Moreover, it has been shown in the literature that the scalar fields generated by LDs accurately identify invariant phase-space structures—such as equilibria, stable and unstable manifolds, invariant tori, and periodic orbits—that govern the dynamical evolution of trajectories [34, 28].

Computationally, the implementation of LDs is straightforward, since the integrals in Eq. (4) can be reformulated as an initial value problem using the Fundamental Theorem of Calculus. For example, for the forward component of the Lagrangian descriptor we can write:

$$\begin{cases} \frac{d\mathcal{L}_f}{d\tau} = \mathcal{F}(\mathbf{x}(t_0 + \tau; \mathbf{x}_0), t_0 + \tau) \\ \mathcal{L}_f(\mathbf{x}_0, t_0, 0) = 0 \end{cases} \quad (5)$$

which we can easily solve simultaneously with the equations of motion in Eq. (1) that govern the evolution of the trajectory.

## 2.2 Time-averaged arclength in the frequency domain

In this subsection we introduce the time-averaged arclength of a trajectory starting at the initial condition  $\mathbf{x}_0$  at time  $t = t_0$ , which is given by:

$$\Omega = \frac{\mathcal{L}_f(\mathbf{x}_0, t_0, \tau)}{\tau}. \quad (6)$$

We claim that this quantity, derived from Lagrangian descriptors, contains enough dynamical information to determine whether a trajectory in a Hamiltonian system is chaotic or regular. Note that this chaos indicator requires only forward-time integration of the trajectory, since backward integration would yield the same dynamical classification.

The motivation behind the definition provided in Eq. (6) is based on a similar chaos indicator that we investigated in [23] using the LD framework, where we proved that if one defines the difference between the forward LD value of two neighboring orbits:

$$\Delta\mathcal{L} = |\mathcal{L}_f(\mathbf{x}_0) - \mathcal{L}_f(\mathbf{x}_0 + \delta\mathbf{x})|, \quad (7)$$

where  $\delta\mathbf{x} \in \mathbb{R}^N$  is a vector in the phase space of the system with a random direction that satisfies  $\|\delta\mathbf{x}\| \ll 1$ , this indicator allows us to easily and accurately classify  $\mathbf{x}_0$  as either chaotic or regular. In that work we showed that for a regular initial condition,  $\Delta\mathcal{L}$  is upper bounded by a linear function in time:

$$\Delta\mathcal{L}_{\text{reg}} \leq \mathcal{C}\|\delta\mathbf{x}\|\tau, \quad (8)$$

where  $\mathcal{C}$  is a constant that depends on the dynamical system under analysis. Hence, the asymptotic behavior of the time-averaged  $\Delta\mathcal{L}$ , as  $\tau$  goes to infinity, must be a non-negative constant  $\nu$ :

$$\frac{\Delta\mathcal{L}_{\text{reg}}}{\tau} \sim \mathcal{C}\|\delta\mathbf{x}\| = \nu. \quad (9)$$

This result follows from Birkhoff's Ergodic Partition Theorem [58, 38]. The theorem states that, in the limit  $\tau \rightarrow \infty$ , time averages of positive functions along trajectories of dynamical systems defined on compact sets and preserving smooth measures do exist. Moreover, the level sets of these limiting functions form invariant sets. Since Hamiltonian systems preserve phase-space volume, they also preserve smooth measures, and the theorem therefore applies directly. This connection between Lagrangian descriptors and ergodic partitions in Hamiltonian systems has been reported previously in the literature [29, 43, 42].

On the other hand, for a chaotic orbit, we obtained in [23] that the upper bound:

$$\Delta\mathcal{L}_{\text{chaos}} \leq \mathcal{C}\|\delta\mathbf{x}\| \frac{\exp(\lambda_{\max}\tau) - 1}{\lambda_{\max}}, \quad (10)$$

holds, where  $\lambda_{\max}$  is the maximum Lyapunov exponent. As  $\tau$  gets larger, the exponential behavior will dominate, leading to the following asymptotic behavior:

$$\frac{\Delta\mathcal{L}_{\text{chaos}}}{\tau} \sim \mathcal{C}\|\delta\mathbf{x}\| \left( 1 + \frac{\lambda_{\max}}{2}\tau + \sum_{i=2}^{\infty} \frac{\lambda_{\max}^i}{(i+1)!}\tau^i \right), \quad (11)$$

which for short integration times will exhibit linear behavior ( $\lambda_{\max}\tau \ll 1$ ). Note that for the regular case we have  $\lambda_{\max} = 0$ , and we recover the expression given in Eq. (9).

Using Birkhoff's Ergodic Partition Theorem we can thus deduce that the time-averaged LD  $\Omega$  introduced in Eq. (6) will converge to a non-negative constant  $\xi$  as time goes to infinity for a regular trajectory, that is:

$$\Omega_{\text{reg}} = \frac{\mathcal{L}_f}{\tau} \sim \xi \geq 0. \quad (12)$$

Conversely, for chaotic trajectories, it is well known that the behavior over time is different from a constant without any clear trend [29, 43, 42]. Fig. 1 (A) displays the evolution of  $\Omega$  for an ensemble of 5000 trajectories in the Hénon-Heiles system (see Eq. (15)) at an energy  $\mathcal{H} = 1/8$ . In it, two distinct behaviors are evident. For chaotic trajectories, the values of  $\Omega$  remain confined between the two sets that correspond to regular orbits. This is consistent with the known topological structure of Hamiltonian systems with 2 degrees of freedom, where the evolution of chaotic orbits is bounded by KAM tori. By plotting the values of  $\Omega$  on the  $y - p_y$  Poincaré section in Fig. 1 (B), we confirm that trajectories identified as chaotic by  $\Omega$  are mapped to the chaotic sea while those considered regular correspond to the regular islands.

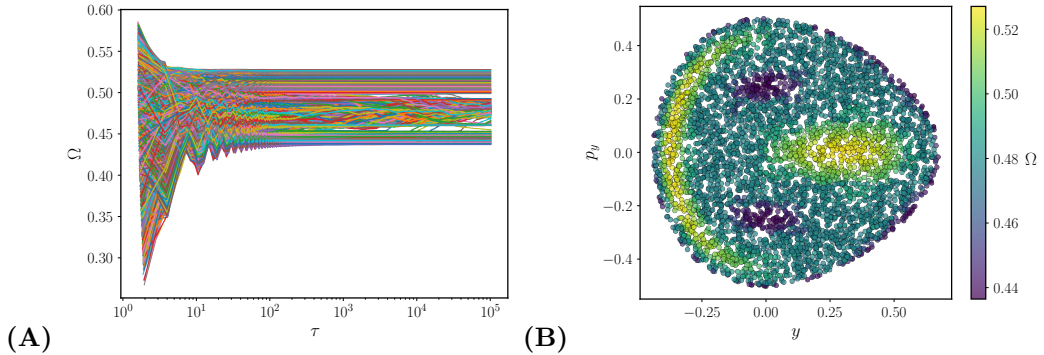
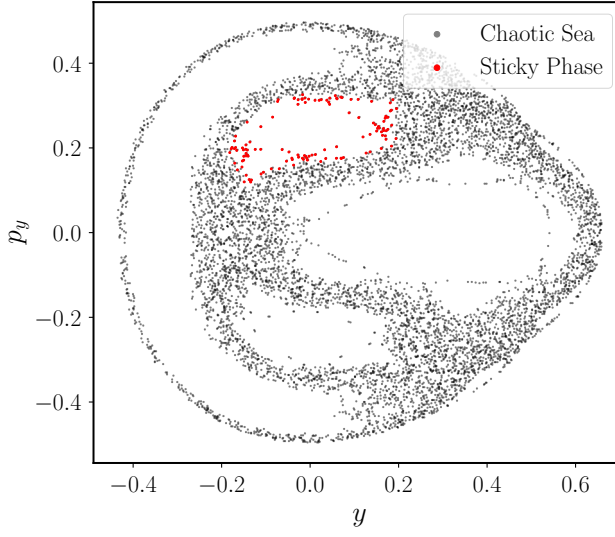


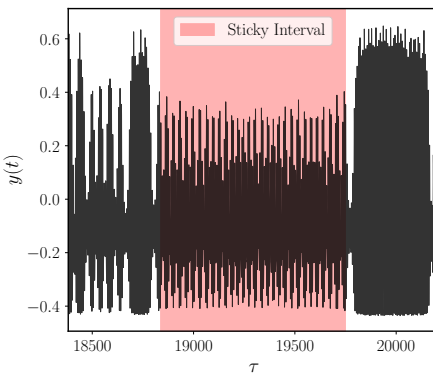
Figure 1: Illustration of Birkhoff's Ergodic Partition Theorem using  $\Omega$  in the Hénon-Heiles system. (A) Time evolution of  $\Omega$  for an ensemble of 5000 trajectories in the Hénon-Heiles system whose total energy is  $\mathcal{H} = 1/8$ . (B) Value of  $\Omega$  for the same ensemble of initial conditions depicted in the Poincaré section given by  $x = 0$  and  $p_x > 0$  (shown in Fig. 4). Panel (A) shows that the chaotic initial conditions (according to the criteria given for  $\Omega$ ) are confined between two regimes of regular trajectories. This is consistent with Birkhoff's Ergodic Partition Theorem for systems with 2 degrees of freedom. Furthermore, the value of  $\Omega$  effectively identifies the different structures present in the system's phase space, as it can be seen in panel (B).

The behavior observed in the time-averaged LD values of chaotic trajectories arises from *dynamical stickiness* [36], a phenomenon typical of systems with mixed phase space, where regular and chaotic regions coexist. During its exploration of phase space, a chaotic trajectory may approach a regular region and display quasi-regular motion for finite time intervals. This intermittent behavior generates long-term temporal correlations along the trajectory, distinguishing it from a purely random or uniformly hyperbolic process [36, 1]. This dynamical regime is illustrated for an example orbit in the Hénon-Heiles system in Fig. 2. In Fig. 2 (A), the red dots indicate points where the chaotic trajectory evolves near a regular island. Panels (B) and (C) show the time evolution of the coordinate  $y(t)$  and momentum  $p_y(t)$ , respectively, during the interval in which dynamical stickiness occurs. During this period, both quantities exhibit quasi-regular oscillations before the trajectory returns to fully chaotic motion.

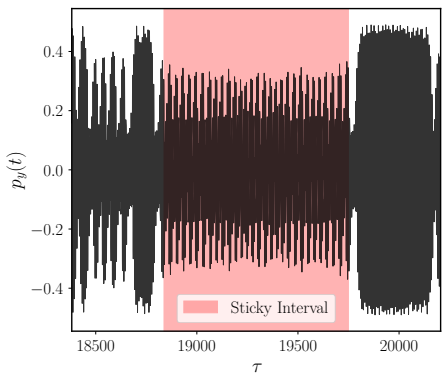
To gain further insight into this transient regularization, we analyzed the dynamics in the frequency domain. In Figs. 3 (A) and (B), the Fourier Transform (FT) of the coordinates  $y(t)$  and  $p_y(t)$  are depicted, respectively. From the analysis of these time series it is clear that there is a significant difference in the spectral domain for the evolution in the chaotic sea (orange) and the evolution near the regular island (blue). Furthermore, these panels depict the already known behavior for a chaotic trajectory in the frequency domain, which is a broadband spectrum, while for the quasi-regular phase undergone by the trajectory, the spectrum shows significant lower spectral power and sharper spectral lines.



(A)

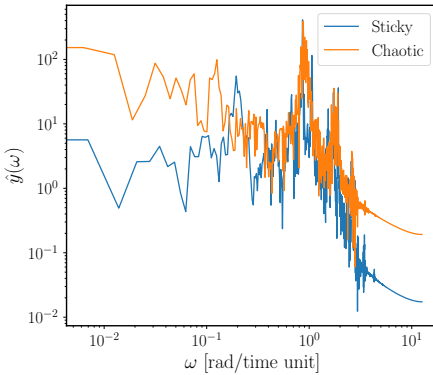


(B)

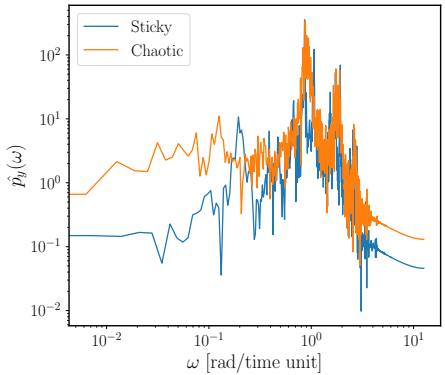


(C)

Figure 2: Dynamical stickiness in the Hénon-Heiles system. (A) Intersections of a chaotic trajectory with the Poincaré section defined by  $x = 0$  and  $p_x > 0$ . The gray points belong to the chaotic sea, while the red points correspond to the sticky regime, where the trajectory lingers near the boundaries of a regular island. (B) and (C) Time series of  $y(t)$  and  $p_y(t)$  during the sticky interval. Note the quasi-regular oscillations observed within this interval before the trajectory diffuses back into the chaotic sea.



(A)



(B)

Figure 3: Spectral signatures of dynamical stickiness. Fourier transform computed for (A) the coordinate  $y(t)$  and (B) the momentum  $p_y(t)$ . The blue curves correspond to the spectral analysis of the trajectory during the sticky interval, as shown in Fig. 2, while the orange curves represent the behavior in the chaotic sea. The comparison reveals that the motion during the sticky interval exhibits sharp spectral lines, in contrast with the broad spectrum characteristic of chaotic motion.

Since the behavior of  $\Omega$  differs significantly between regular and chaotic trajectories, it can serve as a chaos indicator on its own. To characterize it further, we can examine  $\Omega$  in the frequency domain. For a regular trajectory, the Fourier transform of  $\Omega$  produces a Dirac delta function, indicating that the power of the time series is concentrated at low frequencies:

$$\hat{\Omega}_{\text{reg}} = \xi \delta(\omega). \quad (13)$$

Since experimentally measured time series are finite, the spectral signature of a regular trajectory will not appear as a perfect delta function but rather as a sinc function. In contrast, for a chaotic orbit,  $\Omega$  exhibits an inverse power-law behavior in the frequency domain [48]. This corresponds to the Fourier transform of a finite time series generated by a polynomial-like function, and therefore:

$$\hat{\Omega}_{\text{chao}} \sim \omega^{-1}. \quad (14)$$

This difference in the spectral signature makes  $\Omega$  to be the simplest geometrical chaos indicator derivable from LDs and proves that the mathematical framework of Lagrangian descriptors is robust and self-contained for the analysis of chaotic and regular behavior in Hamiltonian systems.

### 3 Results

In this section, we present the results obtained by applying the time-averaged Lagrangian descriptor,  $\Omega$ , to characterize the chaotic or regular nature of trajectories in two well-known systems: the Hénon–Heiles [19] and Fermi–Pasta–Ulam (FPU) [12] models. We evaluate the performance of  $\Omega$  and its Fourier transform,  $\hat{\Omega}$ , in detecting chaotic and regular behavior under different experimental setups by comparing our results with SALI and GALI, which serve as ground-truth chaos indicators.

The Hénon–Heiles system is a two-degree-of-freedom Hamiltonian given by

$$H(x, y, p_x, p_y) = \frac{p_x^2}{2} + \frac{p_y^2}{2} + \frac{1}{2}(x^2 + y^2) + x^2y - \frac{1}{3}y^3, \quad (15)$$

while the FPU lattice with  $N$  degrees of freedom is described by

$$H(\mathbf{q}, \mathbf{p}, k, \alpha, \beta) = \sum_{i=1}^N \frac{p_i^2}{2} + \frac{k}{2} \sum_{i=1}^N (q_{i+1} - q_i)^2 + \frac{\alpha}{3} \sum_{i=1}^N (q_{i+1} - q_i)^3 + \frac{\beta}{4} \sum_{i=1}^N (q_{i+1} - q_i)^4, \quad (16)$$

where  $k, \alpha$  and  $\beta$  are the system parameters.

#### 3.1 Numerical validation in benchmark Hamiltonian models

To validate our theoretical predictions regarding the behavior of  $\Delta\mathcal{L}$  and  $\Omega$  indicators, we begin by analyzing the Hénon–Heiles system with them. To do so, we have chosen two representative initial conditions, one regular (blue) and one chaotic (orange) located on the Poincaré section defined by  $x = 0$  and  $p_x > 0$  for a total energy  $\mathcal{H} = 1/8$ . These initial conditions are overlaid on the section, shown in Fig. 4. Furthermore, this figure can be used to corroborate the results we presented in Fig. 1 (B), confirming the effectiveness of  $\Omega$  in correctly mapping trajectories to the correct phase space regions according to their dynamical behavior.

Fig. 5 (A) presents the evolution of the  $\Delta\mathcal{L}$  indicator for a regular (blue) and a chaotic (orange) initial condition, computed with an initial separation of  $\|\delta\mathbf{x}\| = 10^{-8}$ . Analogous results obtained with a smaller initial separation of  $\|\delta\mathbf{x}\| = 10^{-12}$  are shown in Fig. 5 (C). All the four trajectories involved in the calculation of  $\Delta\mathcal{L}$  were integrated for a total time  $\tau = 10^5$  with the Dormand-Prince 8(9) ODE solver [46] implemented in the PYTHON package SciPy [62], ensuring a conservation of energy within to  $10^{-9}$ , achieved setting the relative and absolute tolerances to  $10^{-10}$ .

Consistent with the prediction given in Eq. (8), the regular trajectory exhibits a clear linear growth in time while for the chaotic initial condition,  $\Delta\mathcal{L}$  diverges by several orders

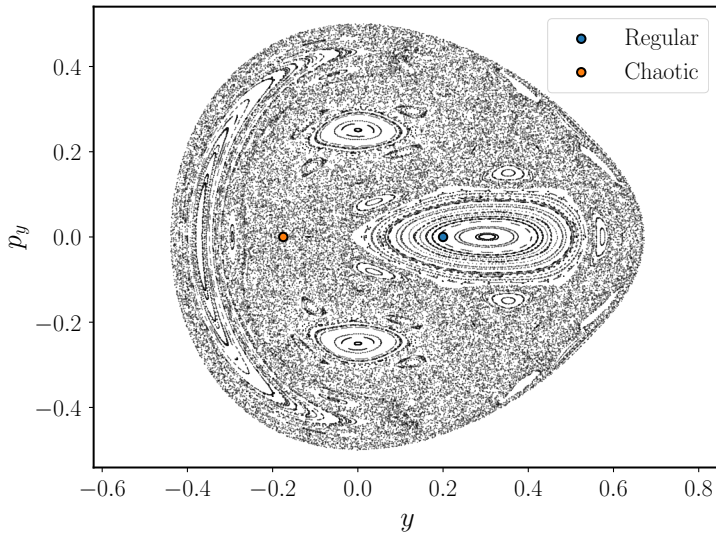


Figure 4: Poincaré Section of the Hénon-Heiles System. Poincaré section defined by  $x = 0$  and  $p_x > 0$  for the Hénon-Heiles, given in Eq. (15), at a total energy  $\mathcal{H} = 1/8$ . A regular (blue) and a chaotic (orange) initial condition are overlaid, illustrating the mixed phase space structure. These two representative initial conditions were selected to validate the performance of the chaos indicator  $\Omega$ .

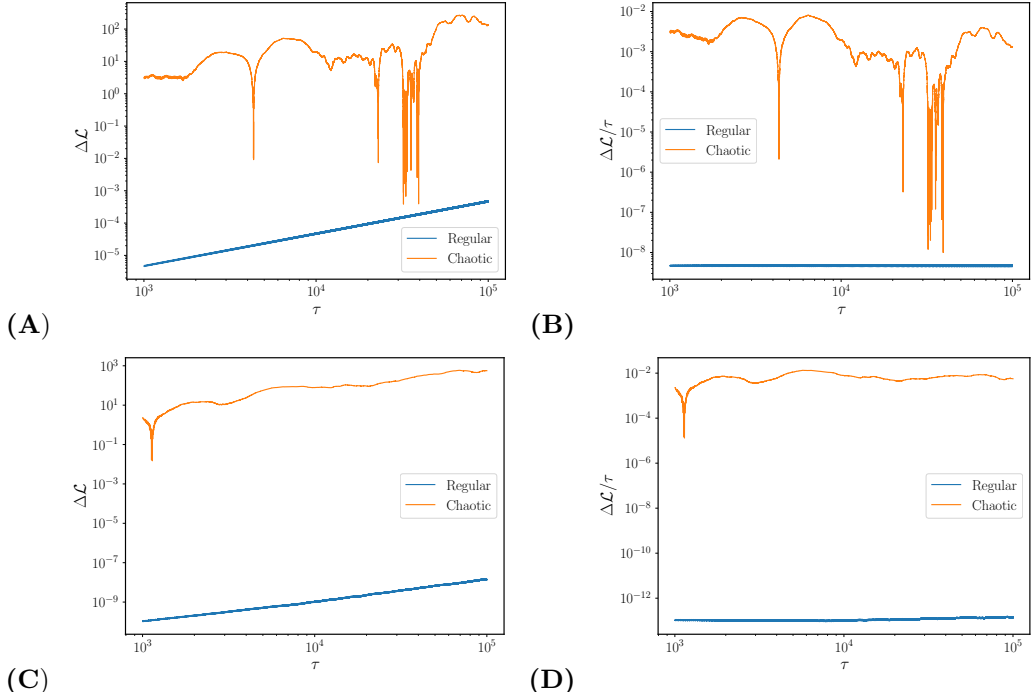


Figure 5: Evolution of  $\Delta\mathcal{L}$  and its time average in the Hénon-Heiles system. (A) Time evolution of the  $\Delta\mathcal{L}$  indicator, defined in Eq. (7), for a regular (blue) and a chaotic (orange) initial condition of the Hénon-Heiles system computed with  $\|\delta\mathbf{x}\| = 10^{-8}$ . (B) Corresponding time evolution of the time-averaged  $\Delta\mathcal{L}$  chaos indicator, computed under the same conditions, for the same two trajectories. (C) and (D) Analogous results computed with and initial separation  $\|\delta\mathbf{x}\| = 10^{-12}$ . Note that the regular trajectory exhibits linear growth, resulting in a constant average.

of magnitude. These results are in perfect agreement with the theoretical bounds derived in Sec. 2.2. For an even clearer distinction between both dynamical regimes, it is convenient to examine the time-averaged  $\Delta\mathcal{L}$  indicator. For the regular trajectory, it converges to a constant very close to the value of the initial separation  $\|\delta\mathbf{x}\|$  that was chosen to compute it, as supported by Fig. 5 (B) and (D). Since this asymptotic behavior is directly proportional to  $\|\delta\mathbf{x}\|$ , it will vanish if we take the limit  $\|\delta\mathbf{x}\| \rightarrow 0$ , recovering the known result from Birkhoff's Ergodic Partition Theorem.

On the other hand, for the chaotic orbit, the asymptotic behavior is given in Eq. (11). Due to the relatively short integration times considered for the analysis, the evolution is dominated by the linear term in the expansion as the higher order terms in  $\exp(\lambda_{\max}\tau)$  are suppressed due to higher powers of  $\lambda_{\max}$ , which for this orbit is approximately 0.04. However,  $\Delta\mathcal{L}$  will eventually diverge exponentially when the integration time is large enough to compensate the small value of the maximum Lyapunov exponent of the orbit.

After having analyzed the numerical results for the  $\Delta\mathcal{L}$  indicator in the time domain, and observing that they are in good agreement with the theoretical estimations presented in Sec. 2.2, Fig. 6 shows the time evolution of the time-averaged LD ( $\Omega$ ) for both trajectories. For the regular trajectory, depicted in blue, it is clear that it converges to a constant as it is predicted by Birkhoff's Ergodic Partition Theorem, which is a known result previously reported in [29, 43, 42]. Regarding the chaotic trajectory, presented in orange, its time evolution exhibits persistent aperiodic fluctuations without a discernible pattern.

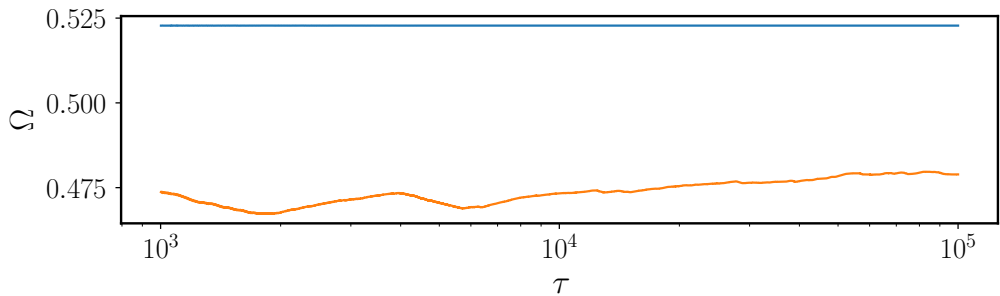


Figure 6: Time evolution of  $\Omega$  in the Hénon-Heiles system. Evolution of the time-averaged Lagrangian descriptor  $\Omega$ , defined in Eq. (12), for a regular (blue) and a chaotic (orange) initial condition in the Hénon-Heiles system. The convergence to a regular value in the case of the regular trajectory is consistent with Birkhoff's Ergodic Partition Theorem, whereas the chaotic trajectory exhibits persistent fluctuations.

To better characterize the signatures of  $\Omega$  for regular and chaotic motion, it is convenient to explore its behavior in the frequency domain, as in Sec. 2.2 we derived the expected spectral characteristics for both dynamical regimes. Fig. 7 shows the magnitude of  $\Omega$ 's Fourier transform, computed using the Fast Fourier Transform (FFT) algorithm [5]. Two key spectral features become evident. First, for the chaotic orbit, the resulting spectrum depicted in orange presents a  $1/\omega$  power law scaling as the theory predicts, which comes from the asymptotic trend given in Eq. (11), as from it we know that  $\Omega$  is related to a finite time-series generated by a polynomial, whose Fourier Transform is known to be an inverse-power law, matching our observations. Secondly, the regular trajectory shows a lower magnitude and a less noisy spectrum, concentrated towards low frequencies. This is a consequence of having a constant signal over a finite time interval, as this is equivalent to a windowed function with a constant value, whose FT is not a Dirac delta function, but rather a sinc function. These results perfectly match the already known results in the field for the frequency analysis of regular and chaotic motion in Hamiltonian systems.

In spite of being helpful to visualize the spectral content of  $\Omega$ , the FFT produces undesirable noise at high frequencies that might difficult the distinction between regular and chaotic trajectories via spectral analysis. One of the existing procedures that can be used to improve the results obtained with the FFT (removing noise and increasing the spectral separation) is to calculate the Power Spectral Density (PSD) using Welch's method [63],

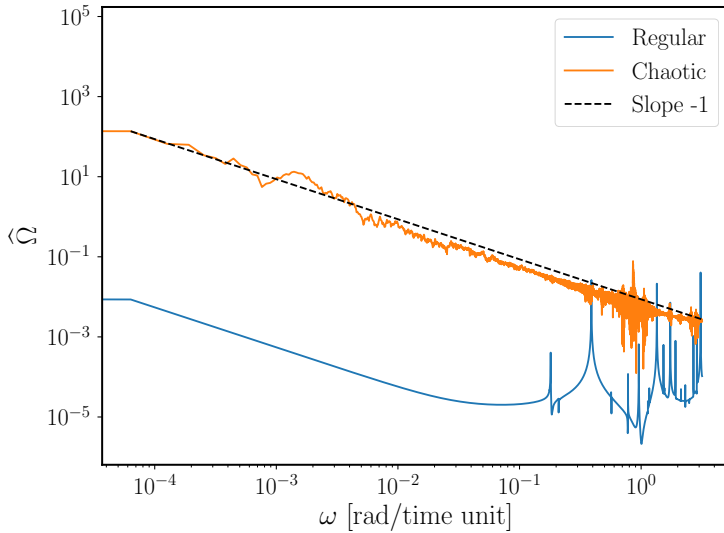


Figure 7: Spectral analysis of  $\Omega$ . Magnitude of the Fourier Transform the time-averaged Lagrangian descriptor for a regular (blue) and a chaotic (orange) initial condition in the Hénon-Heiles system. The dashed black line represents the theoretical  $1/\omega$  scaling, confirming the inverse power-law behavior expected for chaotic dynamics.

which is based on Bartlett's method (also known as the method of averaged periodograms) [2].

The PSD of a time-series  $x[n]$  using Welch's method is computed as follows:

1. The signal  $x[n]$  is split into  $L$  overlapping segments of length  $N$ , with  $D$  overlapping points. Note that if  $D = 0$ , we recover Bartlett's method, where the signal is split in non-overlapping segments.
2. The overlapped segments are windowed by a function  $w[n]$  [18, 44], yielding a windowed function in time:

$$x_w[n] = x[n] \cdot w[n], \quad \text{with } 0 \leq n \leq N-1. \quad (17)$$

For the present work, we have used the Hann window, defined as:

$$w_{\text{Hann}}[n] = \frac{1}{2} \left[ 1 - \cos \left( \frac{2\pi n}{N} \right) \right] = \sin^2 \left( \frac{\pi n}{N} \right), \quad \text{with } 0 \leq n \leq N-1. \quad (18)$$

Windowing a function results in the loss of information at the edges of the signal, which is mitigated by overlapping the individual segments in time. It is this windowing step that makes Welch's method differ from Bartlett's method, as the windowed function produces what is known as a modified periodogram.

Once the above steps have been carried out, the power spectrum of each segment is computed by squaring the magnitude of the Discrete Fourier Transform (DFT). Lastly, the individual spectrum results are averaged, resulting in power measurement with reduced variance (less noise). The numerical implementation used is done in the PYTHON package SciPy [62].

The resulting PSDs for the two initial conditions that we have chosen to illustrate the procedure are shown in Fig. 8. The result for the regular trajectory (blue) shows a smooth decay towards high frequencies, as we have seen in Fig. 7, where the sharp peaks present for  $\omega > 0.1$  are attributable to the finite precision of the ODE solver and are not a characteristic of the dynamical evolution of the trajectory. The PSD of the chaotic trajectory (orange) has spectral content along a broader range of frequencies, which is the known result for chaotic

regimes. Using Welch's method, it is clear that power for the regular orbit is concentrated towards low frequencies while the chaotic one exhibits a broad spectrum, providing a wider separation between both PSDs compared to what is obtained with the FFT as it was shown in Fig. 7.

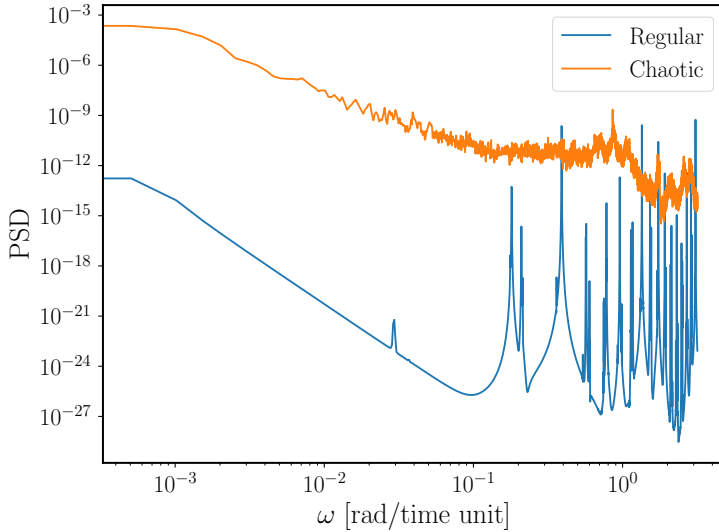


Figure 8: Enhanced spectral separation using Welch's method. Power Spectral Density (PSD) computed for a regular (blue) and a chaotic (orange) trajectory using Welch's method [63]. Compared to the results obtained with the FFT of the full time-series (shown in Fig. 7), this technique yields a significantly cleaner signal and improves the separation between the regular and chaotic regimes, facilitating the identification of the trajectory's dynamical nature.

To demonstrate the robustness of  $\Omega$ , we have analyzed chaos and regularity in the ensemble of trajectories shown in Fig. 1 (A) with it and with the Smaller Alignment Index (SALI) computed using the PYTHON package Chaoticus [24]. The Power Spectral Density analysis (Fig. 9 (B)) reveals a clear separation at low frequencies, which allows the generation of a histogram based only on the zero-frequency component (Fig. 9 (C)), which presents a clear, separable bimodal distribution. Additionally, it is also possible to define the spectral concentration metric, obtained as the ratio of the zero-frequency component and the rest of the significant frequencies present in the signal (Fig. 9 (D)). Moving now to the time domain, the coefficient of variation defined as:

$$c_v = \frac{\sigma(\Omega)}{\mu(\Omega)}, \quad (19)$$

can also be used to distinguish among the two regimes. Lastly, as a ground truth reference, in Fig. 9 (E) the histogram generated by it is presented. Note that unlike SALI, which suffers from exponential decay leading to machine precision limits for chaotic orbits (feature also presented by GALI), the different metrics based on  $\Omega$  remain stable, making them ideal features for training symplectic neural networks and classifiers. For the ensemble we have considered as a test case, SALI classified 59.3 % of the trajectories as chaotic. Taking this as the true percentage of chaotic orbits that are present in the data set, using the thresholds depicted in the different panels for each of the methods, we found that using the zero-frequency metric 58.44 % of the trajectories were classified as chaotic, while using the spectral concentration metric we obtained 60.58 % and with the coefficient of variation it was 58.44 %. This shows that  $\Omega$  has great accuracy and that the classification can be better performed using the zero-frequency component or the coefficient of variation rather than the spectral concentration as the first two produce separable bimodal distributions. Note that even though  $\Omega$  did not produce a perfect classification, due to its ability to generate very large datasets, the small amount of wrongly classified initial conditions will actually not be relevant for the overall performance of the classification.

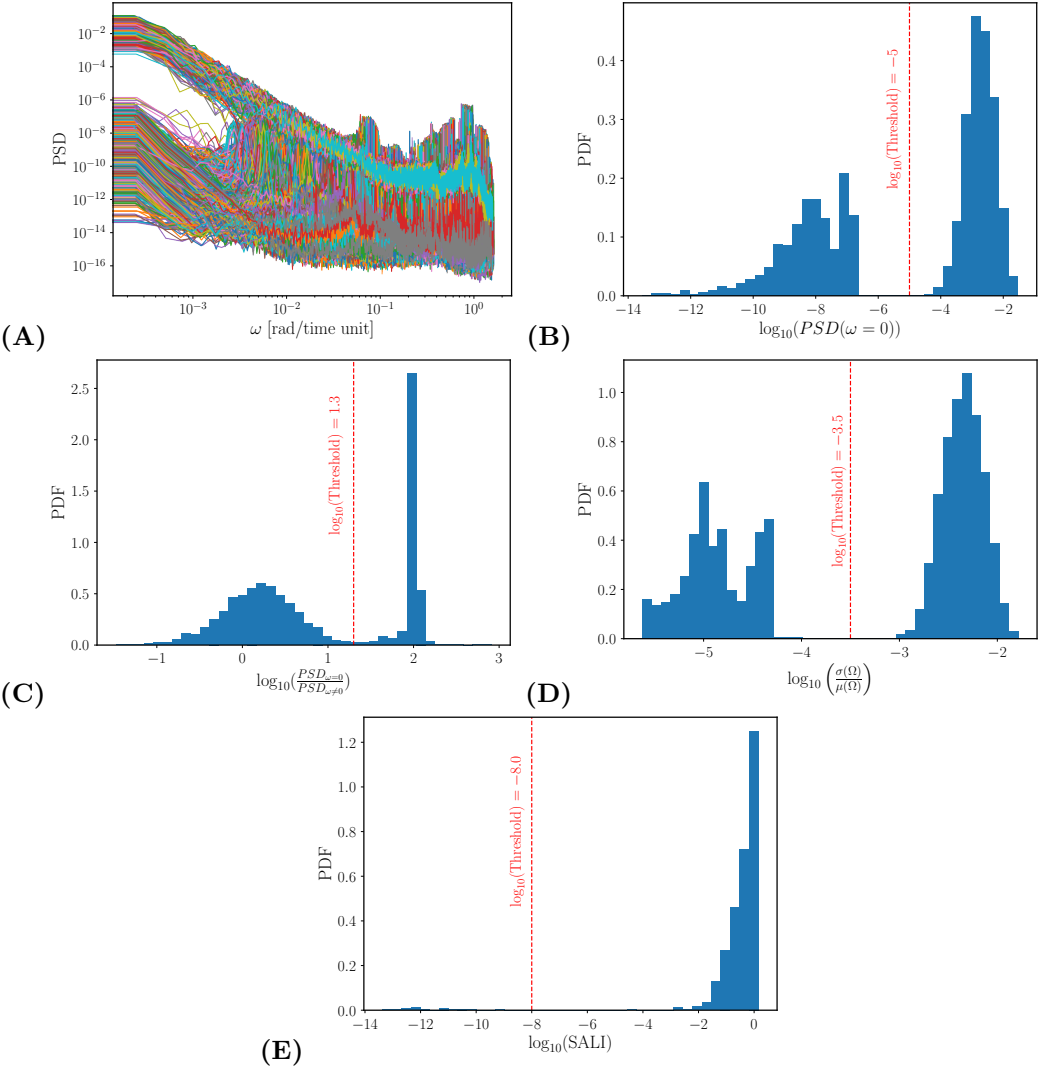


Figure 9: Comparison of classification methodologies. **(A)** Power Spectral Density of  $\Omega$  for the trajectory ensemble depicted in Fig. 1 **(A)**, computed using Welch's method. At low frequencies ( $\omega \rightarrow 0$ ), a clear separation among the two dynamical regimes is evident, with higher PSD values corresponding to chaotic trajectories. The high frequency range is dominated by numerical error and is therefore excluded from the analysis. **(B)** Histogram of the zero-frequency (DC) component from panel **(A)**. The red dashed vertical line marks the threshold that separates regular from chaotic motion. **(C)** Histogram of the spectral concentration (ratio of the DC component to the total PSD in the valid frequency range). **(D)** Histogram of the coefficient of variation  $c_v = \sigma/\mu$  of  $\Omega(t)$ . Since for regular trajectories  $\Omega \sim \xi \in \mathbb{R}^+$ , they exhibit low  $c_v$  values, while higher values can be linked to chaotic behavior. **(E)** Histogram of the SALI indicator, defined in Eq. (23). Note that for chaotic motion, SALI decays rapidly to zero, causing these points to not be displayed in the histogram due to the log scale.

Since the theoretical derivation of  $\Omega$  assumes no explicit functional form of the Hamiltonian, the method is system and dimension independent. This makes it natural to apply this methodology to higher dimensional systems and analyze their dynamical behavior, which if it was going to be done via the traditional approaches will be tremendously inefficient. To exemplify the advantages that  $\Omega$  offers as a chaos indicator, we have applied it to the Fermi-Pasta-Ulam system given in Eq. (16). For it, we have analyzed the behavior of  $\Omega$  in both, the time and the frequency domains as we previously did for the Hénon-Heiles system. Fig. 10 (A) shows the time evolution of  $\Omega$  for a regular (blue) and a chaotic (orange) orbit in the FPU with 8 degrees of freedom, where the same behavior observed in Fig. 5 for Hénon-Heiles is also seen in this case, corroborating our claim that the behavior of  $\Omega$  is system and dimension independent. Analyzing the two time series in the frequency domain with the FFT (Fig. 10 (B)) and Welch's method (Fig. 10 (C)), we have found the same functional behavior as we did for the Hénon-Heiles system and what was theoretically established in Sec. 2.2.

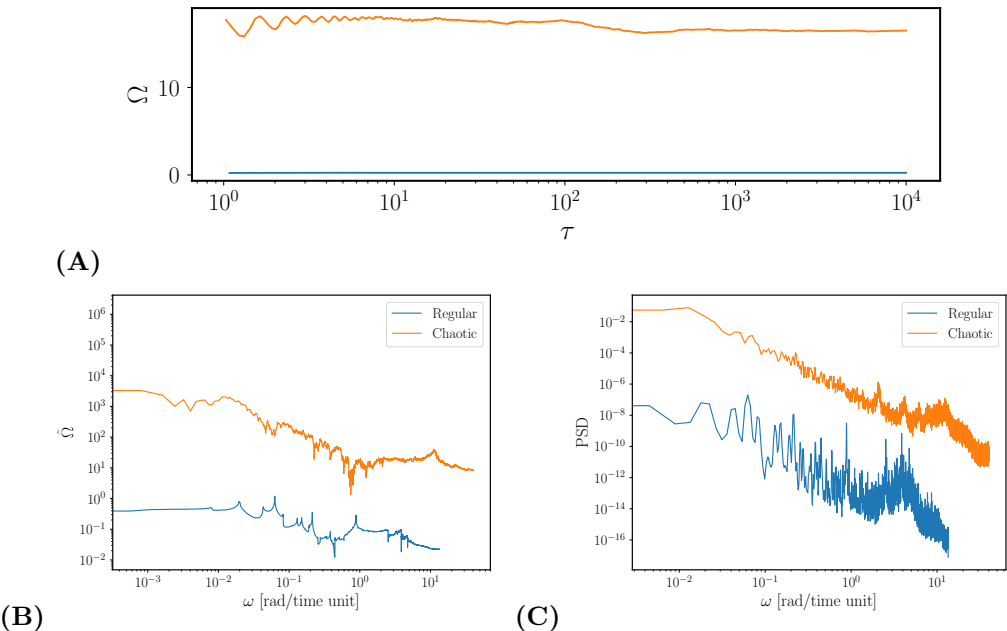


Figure 10: Analysis of  $\Omega$  in the Fermi-Pasta-Ulam (FPU) system with  $N = 8$ . (A) Time evolution of  $\Omega$  for a regular (blue) and a chaotic (orange) initial condition in the FPU system. (B) Fourier Transform of the time-series generated by  $\Omega$  and depicted in panel (A). (C) Power Spectral Density (PSD) of the same time-series computed using Welch's method. As it can be seen, the behavior of  $\Omega$  is analogous to the one found for the Hénon-Heiles system, confirming it's independence from the system's dimensionality. The regular initial condition is defined by  $q_i = 0.1$  and  $p_i = 0$  for  $i = 1, \dots, 8$ , while the chaotic initial condition is given by  $\mathbf{q} = (1.00097, 0, 1.04003, 0, -1.04003, 0, -1.00097, 0)$  and  $\mathbf{p} = (0.57060, 0, -0.57060, 0, 0.57060, 0, -0.57060, 0)$ .

As the computation of  $\Omega$  does not require the variational equations or neighboring orbits, it is expected to present a slower growth when the dimensionality of the system is increased when compared to other chaos indicators. In the present work, we have decided to compare it to the Generalized Alignment Index (GALI). In Sec. A, the reader can find a comprehensive review of GALI and its asymptotic behavior as a function of the system's number of degrees of freedom.

In Fig. 11, the computational time it takes to evolve the system of equations of motion in the case of  $\Omega$  and the system composed of the equations of motion plus 4 sets of variational equations to compute  $\text{GALI}_4$  are presented. In the case of  $\text{GALI}_4$ , the integration time used to simulate all the ODEs was set to  $\tau = 10^3$  units of time whereas for  $\Omega$  it was  $\tau = 10^4$ . This was done to emphasize that  $\Omega$  is considerably faster to compute even for longer integration times. What the results show is clear: computing GALI, and thus any chaos indicator

relying on the variational equations, even for a small number of deviation vectors, becomes computationally impossible for systems with a considerable number of degrees of freedom. This is clear if one fits a second order polynomial for the time it takes to simulate the necessary equations to compute GALI, as we found that this fit yields  $R^2 = 1$ , which is expected as computational complexity, obtained taking into account that with  $k$  deviation vectors one needs  $2N(k + 1)$  (where  $k$  ranges from 2 to  $2N$ ), is  $\mathcal{O}(N^2)$ . On the other hand,  $\Omega$  shows a clear linear growth with  $N$ , yielding a  $R^2 = 0.998$  for a linear fit. This is due to the computational complexity depending only on the equations of motion, and thus the simulation of  $\Omega$  is  $\mathcal{O}(N)$ . Note that this reduction in computational complexity is what solves the problem with high dimensional problems as  $\Omega$  does not introduce any additional complexity to the simulation of the system.

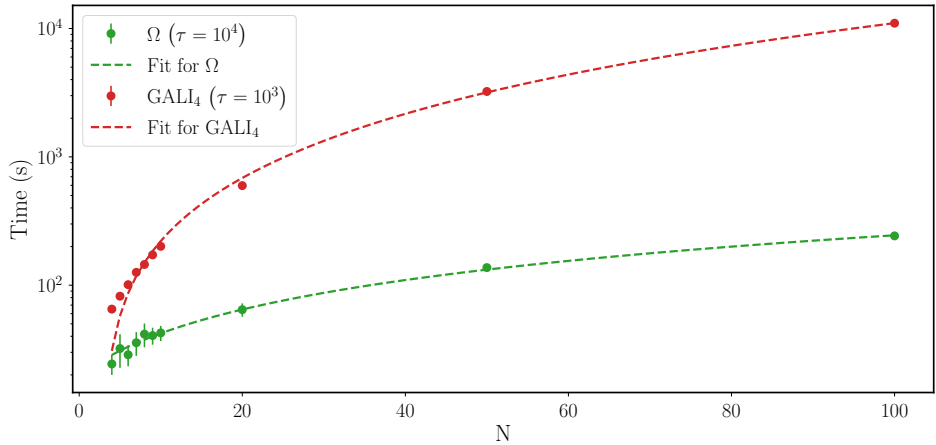


Figure 11: Computational time scaling for  $\Omega$  and  $\text{GALI}_4$  in the Fermi-Pasta-Ulam (FPU) system. The plot compares the wall-time required to integrate the ODEs for the calculation of  $\Omega$  (only the equations of motion) versus  $\text{GALI}_4$  (equations of motion coupled with variational equations) as a function of number of degrees of freedom  $N$ . Integration times were set to  $\tau = 10^4$  for  $\Omega$  and  $\tau = 10^3$  for  $\text{GALI}_4$ . The filled data points represent the average computing time over 100 randomly sampled initial conditions for each  $N$ , with error bars denoting one standard deviation. Note that the additional computational cost of calculating  $\text{GALI}_4$ , often done via Singular Value Decomposition (SVD), is excluded from the comparison. The simulations were performed using an AMD Ryzen 9 7950X 16-Core CPU chip.

### 3.2 Methodology for chaos detection

Finally, in this subsection we present an overview of the different possibilities that exist at the time of analyzing the existence of chaos and regularity in Hamiltonian system using the methods introduced in this work.

In the case where one specific trajectory is being analyzed, the best option to determine its nature is to compute the FFT and check if the resulting spectrum matches the spectral signatures known for chaos or regularity. On the other hand, in order to produce a detail analysis of a system, one will need to explore its phase space, meaning that an ensemble of initial conditions must be analyzed. In this situation, one can analyze the time series obtained after the integration of the equations of motion in the time domain using the coefficient of variation, defined in Eq. (19). In this scenario, regular orbits are characterized by low values of  $c_v$  as for them  $\Omega$  asymptotically approaches a constant value, whereas for a chaotic orbit, fluctuations in the time evolution of  $\Omega$  are present. The other option is to move the analysis to the frequency domain and use the spectral separation present in the PSD to generate a bimodal distribution or measure the spectral concentration of the signal. This process is summarized in the flowchart shown in Fig. 12.

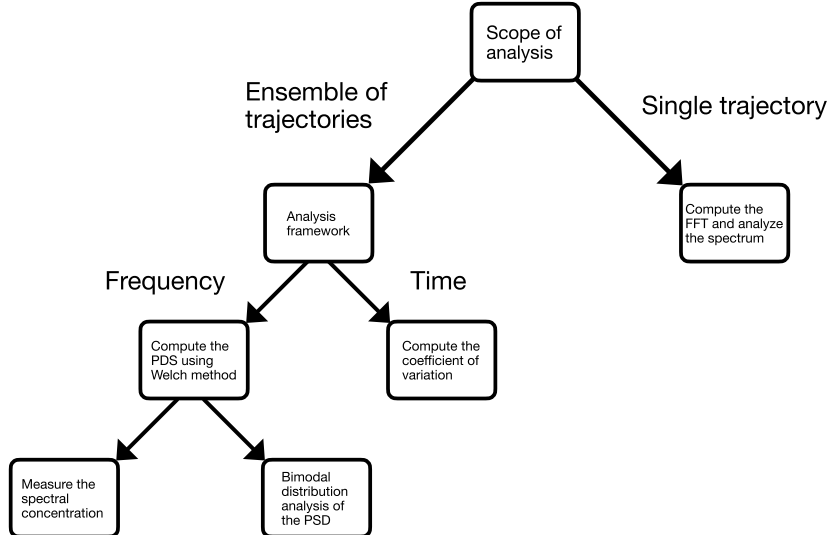


Figure 12: Decision tree for trajectory classification using  $\Omega$ . The flowchart outlines the different possible approaches for distinguishing among regular and chaotic dynamics depending on the scope of the analysis. For single trajectories, the method relies on the analysis of the spectral signature obtained via the FFT. In the case of ensemble of multiple trajectories, the analysis can be performed in the time domain using the coefficient of variation, or in the frequency domain via the spectral concentration or the bimodal analysis of the PSD.

## 4 Conclusions

In this work we have presented rigorous theoretical and numerical arguments to show that the time-average of the Lagrangian descriptor,  $\Omega$ , is a self-contained and efficient chaos indicator for Hamiltonian systems. Unlike traditional variational methods, that rely on the computationally expensive evolution of tangent vectors, or other chaos indicators based on LDs that require information from neighboring orbits, we have demonstrated that the scalar time-series produced by the Lagrangian descriptor contains sufficient information to unambiguously distinguish between regular and chaotic dynamics. The most important implication of this work is the scalability. As indicators like GALI scale quadratically ( $\mathcal{O}(N^2)$ ) with the system's size,  $\Omega$  does it linearly ( $\mathcal{O}(N)$ ) as it only requires the integration of the trajectory itself.

Our numerical results on the Hénon-Heiles and Fermi-Pasta-Ulam systems confirm that the spectral analysis of  $\Omega$  successfully reveals the dynamical nature of a trajectory. For regular trajectories, as predicted,  $\Omega$  rapidly converges to a constant value, which is characterized by a delta function in the frequency domain. On the other hand, for chaotic trajectories, the non-constant but rather fluctuating behavior of  $\Omega$  is translated to an inverse power-law in the frequency domain, which is the already known result due to the dynamical stickiness phenomenon that is present in systems with mixed phase spaces.

This spectral distinction constitutes a complete diagnostic framework, as it allows for the detection of chaos with information coming only from the time-evolution of the trajectory. By linking the geometrical properties of the system's phase space to the behavior of the indicator itself, we propose this method as a robust, simplest indicator for the analysis of Hamiltonian systems.

The high efficiency of the methodology presented in this paper opens the door to the characterization of chaos in high-dimensional space, previously considered computationally intractable. Future studies using this framework could address systems that present Arnold diffusion, the analysis of high dimensional systems of practical interest or the generation of classifiers and models that can predict chaotic behavior. These are some of the studies that could be addressed in the future using what has been presented in this work.

## Acknowledgments

The authors would like to acknowledge Prof. José Bienvenido Sáez Landete from Universidad de Alcalá for providing the computational resources used in the work. Javier Jiménez-López acknowledges the fruitful discussion with Prof. José Bienvenido Sáez Landete, that helped to improve the results obtained in this paper.

## Credit authorship contribution statement

**Javier Jiménez López:** Conceptualization, Data curation, Formal analysis, Funding acquisition, Methodology, Investigation, Resources, Software, Validation, Visualization, Writing - original draft, Writing - review & editing. **Víctor J. García-Garrido:** Conceptualization, Data curation, Formal analysis, Funding acquisition, Investigation, Project administration, Methodology, Resources, Software, Supervision, Validation, Visualization, Writing - original draft, Writing - review & editing.

## Data availability

The data that support the findings of this study are available from the corresponding author upon reasonable request.

## A Ground truth chaos indicators

This appendix briefly describes the Smaller Alignment Index (SALI) [51, 53, 54] and the Generalized Alignment Index (GALI) [55, 40, 35]. These two chaos indicators are used as the ground truth to assess the accuracy of the time-averaged arclength  $\Omega$  in classifying trajectories as chaotic or regular, as well as to evaluate its computational performance. For the present analysis, we have calculated both SALI and GALI using the variational equations instead of the more recent definition based on neighboring trajectories [35].

Following the notation used in Eq. (1), the variational equations of a system with  $N$  degrees of freedom, which determine how a small perturbation (deviation vector)  $\delta\mathbf{x}$  evolves over time, can be written in matrix form as:

$$\dot{\delta\mathbf{x}} = J(\nabla^2 H) \delta\mathbf{x}, \quad (20)$$

where the matrix  $J$  is the Poisson matrix given in Eq. (2) and  $\nabla^2 H$  is the Hessian matrix, which contains the second partial derivatives of the Hamiltonian.

In the case of systems with  $N = 2$  degrees of freedom, SALI is particularly well-suited for the task of chaos detection, as it provides a clear separation between both, regular and chaotic behaviors. In order to classify a trajectory using SALI, we have to simultaneously track the evolution of the initial condition  $\mathbf{x}(0)$  and that of two initially orthogonal deviation vectors,  $\mathbf{w}_1$  and  $\mathbf{w}_2$ . As what is needed from the deviation vectors to compute SALI is their direction, we normalize them at every integration step to ensure consistent directionality throughout the evolution and to control exponential growth:

$$\hat{\mathbf{w}}_i(t) = \frac{\mathbf{w}_i(t)}{\|\mathbf{w}_i(t)\|}, \quad i = 1, 2. \quad (21)$$

Introducing the parallel and antiparallel indices:

$$d_+(t) = \|\hat{\mathbf{w}}_1(t) + \hat{\mathbf{w}}_2(t)\|, \quad d_-(t) = \|\hat{\mathbf{w}}_1(t) - \hat{\mathbf{w}}_2(t)\|, \quad (22)$$

SALI is defined as:

$$\text{SALI} = \min\{d_+(t), d_-(t)\}. \quad (23)$$

Then, SALI represents the minimum length, at time  $t$ , of the two diagonals of the parallelogram generated by the two normalized deviation vectors. A schematic of this procedure is shown in Fig. 13.

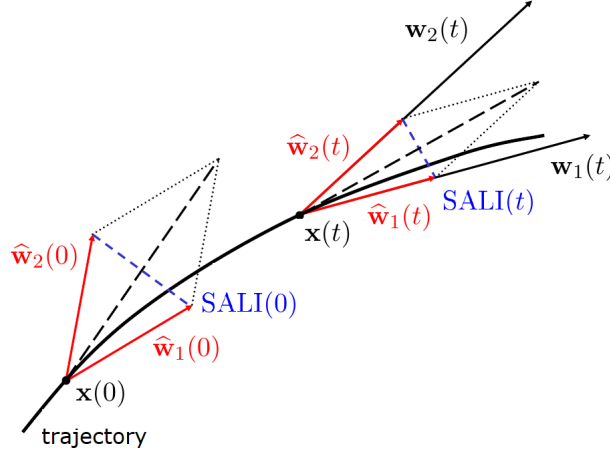


Figure 13: Schematic diagram of SALI. Evolution of a trajectory starting at  $\mathbf{x}(0)$  and of two deviation vectors  $\mathbf{w}_1(t)$  and  $\mathbf{w}_2(t)$  that characterize the behavior of two neighboring trajectories. The SALI indicator at time  $t$  corresponds to the minimum length of the two diagonals of the parallelogram generated by the normalized deviation vectors. Figure adapted from [56].

In the literature it has been shown that for continuous Hamiltonian systems, SALI displays the following asymptotical behaviors [56]:

$$\text{SALI}(t) \propto \begin{cases} \text{constant} & , \text{ for a regular trajectory} \\ e^{-\lambda_{\max} t} & , \text{ for a chaotic trajectory} \end{cases} \quad (24)$$

with  $\lambda_{\max}$  being the largest Lyapunov exponent. These asymptotic behaviors show that for a chaotic trajectory, SALI tends exponential fast to zero, which is a consequence of the deviation vectors aligning with the closest unstable manifold. On the other hand, for a regular trajectory, SALI behaves as a constant. This clear difference in the asymptotic behavior is what makes useful to employ logarithms when working with SALI for the classification.

On the other hand, GALI, which is a generalization of SALI, is defined as follows. For a system with  $N$  degrees of freedom, the GALI of order  $k$ , where  $k$  ranges from 2 to  $2N$ , is obtained through the evolution of  $k$  initially orthogonal deviation vectors  $\mathbf{w}_k(0)$ , which are normalized at every integration step to preserve their direction correctly. Then,  $\text{GALI}_k$  is defined as the volume of the  $k$ -parallelepiped whose edges are the  $k$  unitary deviation vectors. Therefore, it can be calculated using the wedge product:

$$\text{GALI}_k(t) = \|\hat{\mathbf{w}}_1(t) \wedge \hat{\mathbf{w}}_2(t) \wedge \dots \wedge \hat{\mathbf{w}}_k(t)\|. \quad (25)$$

For a regular trajectory whose evolution takes place on an  $s$ -dimensional torus, the asymptotic behavior of  $\text{GALI}_k$  is known to be given by:

$$\text{GALI}_k(t) \propto \begin{cases} \text{constant} & , \text{ if } 2 \leq k \leq s \\ \frac{1}{t^{k-s}} & , \text{ if } s < k \leq 2N - s \\ \frac{1}{t^{2(k-N)}} & , \text{ if } 2N - s < k \leq 2N \end{cases} \quad (26)$$

and in the case of a chaotic trajectory:

$$\text{GALI}_k(t) \propto \exp \left( - \left[ \sum_{j=1}^k (\sigma_1 - \sigma_j) \right] t \right), \quad (27)$$

where  $\sigma_1, \dots, \sigma_k$  are the  $k$ -largest Lyapunov exponents.

## References

- [1] Y. Aizawa, Y. Kikuchi, T. Harayama, K. Yamamoto, M. Ota, and K. Tanaka. Stagnant motions in hamiltonian systems. *Progress of Theoretical Physics Supplement*, 98:36–82, 05 1989. [arXiv:https://academic.oup.com/ptps/article-pdf/doi/10.1143/PTPS.98.36/5369626/98-36.pdf](https://academic.oup.com/ptps/article-pdf/doi/10.1143/PTPS.98.36/5369626/98-36.pdf), doi:10.1143/PTPS.98.36.
- [2] M. S. Bartlett. Smoothing periodograms from time-series with continuous spectra. *Nature*, 161(4096):686–687, 1948. doi:10.1038/161686a0.
- [3] H. Bartosik, Y. Papaphilippou, and A. Wolski. A first taste of nonlinear beam dynamics. In *CAS - CERN Accelerator School 2021: Introduction to Accelerator Physics*, 1 2022. arXiv:2201.01532.
- [4] Z. Chen, J. Zhang, M. Arjovsky, and L. Bottou. Symplectic recurrent neural networks, 2020. URL: <https://arxiv.org/abs/1909.13334>, arXiv:1909.13334.
- [5] J. W. Cooley and J. W. Tukey. An algorithm for the machine calculation of complex fourier series. *Math. Comput.*, 19:297–301, 1965. doi:10.1090/S0025-5718-1965-0178586-1.
- [6] A. Căliman, J. Daquin, and A.-S. Libert. Improved detection of chaos with lagrangian descriptors using differential algebra. *Physica D: Nonlinear Phenomena*, 472:134506, 2025. URL: <https://www.sciencedirect.com/science/article/pii/S0167278924004561>, doi:10.1016/j.physd.2024.134506.
- [7] J. Daquin, R. Pédenon-Orlanducci, M. Agaoglou, G. García-Sánchez, and A. M. Mancho. Global dynamics visualisation from lagrangian descriptors. Applications to discrete and continuous systems. *Physica D: Nonlinear Phenomena*, 442:133520, 2022. doi:10.1016/j.physd.2022.133520.
- [8] S. Das, C. Dock, Y. Saiki, M. Salgado-Flores, E. Sander, J. Wu, and J. Yorke. Measuring quasiperiodicity. *Europhysics Letters*, 114(4):40005, 2016. doi:10.1209/0295-5075/114/40005.
- [9] B. Dietz, A. Heusler, K. H. Maier, A. Richter, and B. A. Brown. Chaos and regularity in the doubly magic nucleus  $^{208}\text{Pb}$ . *Phys. Rev. Lett.*, 118:012501, 2017. doi:10.1103/PhysRevLett.118.012501.
- [10] R. Dvorak, F. Freistetter, and J. Kurths. *Chaos and Stability in Planetary Systems*, volume 683. 2005. doi:10.1007/b94975.
- [11] H. Eleuch and A. Prasad. Chaos and regularity in semiconductor microcavities. *Physics Letters A*, 376(26):1970–1977, 2012. doi:10.1016/j.physleta.2012.04.050.
- [12] E. Fermi, P. Pasta, S. Ulam, and M. Tsingou. Studies of the nonlinear problems. Technical report, Los Alamos National Laboratory (LANL), Los Alamos, NM (United States), 05 1955. URL: <https://www.osti.gov/biblio/4376203>, doi:10.2172/4376203.
- [13] C. Froeschlé, R. Gonczi, and E. Lega. The Fast Lyapunov Indicator: a simple tool to detect weak chaos. Application to the structure of the main asteroidal belt. *Planetary and Space Science*, 45(7):881–886, 1997. doi:10.1016/S0032-0633(97)00058-5.
- [14] C. Froeschlé, E. Lega, and R. Gonczi. Fast Lyapunov Indicators. Application to asteroidal motion. *Celestial Mechanics and Dynamical Astronomy*, 67(1):41–62, 1997. doi:10.1023/A:1008276418601.
- [15] I. Gkolias, J. Daquin, F. Gachet, and A. J. Rosengren. From order to chaos in earth satellite orbits. *The Astronomical Journal*, 152(5), 2016. doi:10.3847/0004-6256/152/5/119.
- [16] I. Gkolias, J. Daquin, D. K. Skoulioudou, K. Tsiganis, and C. Efthymiopoulos. Chaotic transport of navigation satellites. *Chaos: An Interdisciplinary Journal of Nonlinear Science*, 29(10):101106, 2019. doi:10.1063/1.5124682.

[17] S. Greydanus, M. Dzamba, and J. Yosinski. Hamiltonian neural networks. In H. Wallach, H. Larochelle, A. Beygelzimer, F. d'Alché-Buc, E. Fox, and R. Garnett, editors, *Advances in Neural Information Processing Systems*, volume 32. Curran Associates, Inc., 2019.

[18] F. Harris. On the use of windows for harmonic analysis with the discrete fourier transform. *Proceedings of the IEEE*, 66(1):51–83, 1978. [doi:10.1109/PROC.1978.10837](https://doi.org/10.1109/PROC.1978.10837).

[19] M. Hénon and C. Heiles. The applicability of the third integral of motion: some numerical experiments. *Astronomical Journal, Vol. 69, p. 73 (1964)*, 69:73, 1964. [doi:10.1086/109234](https://doi.org/10.1086/109234).

[20] M. Hillebrand, G. Kalosakas, A. Schwellnus, and C. Skokos. Heterogeneity and chaos in the Peyrard-Bishop-Dauxois DNA model. *Phys. Rev. E*, 99:022213, 2019. [doi:10.1103/PhysRevE.99.022213](https://doi.org/10.1103/PhysRevE.99.022213).

[21] M. Hillebrand, S. Zimper, A. Ngapasare, M. Katsanikas, S. Wiggins, and C. Skokos. Quantifying chaos using lagrangian descriptors. *Chaos: An Interdisciplinary Journal of Nonlinear Science*, 32(12):123122, 2022. [doi:10.1063/5.0120889](https://doi.org/10.1063/5.0120889).

[22] J. Jiménez-López and V. J. García-Garrido. Learning the chaotic and regular nature of trajectories in hamiltonian systems with lagrangian descriptors. *Chaos, Solitons & Fractals*, 191:115876, 2025. URL: <https://www.sciencedirect.com/science/article/pii/S0960077924014280>, [doi:10.1016/j.chaos.2024.115876](https://doi.org/10.1016/j.chaos.2024.115876).

[23] J. Jiménez-López and V. J. García-Garrido. A simple chaos indicator based on the lagrangian descriptor difference of neighboring orbits, 2026. URL: <https://arxiv.org/abs/2506.16660>, [arXiv:2506.16660](https://arxiv.org/abs/2506.16660).

[24] J. Jiménez-López, J. Sáez-Landete, and V. J. García-Garrido. Chaoticus: a parallel approach to the computation of chaos indicators, 2025. URL: <https://arxiv.org/abs/2507.00622>, [arXiv:2507.00622](https://arxiv.org/abs/2507.00622).

[25] J. Laskar. Frequency analysis for multi-dimensional systems. global dynamics and diffusion. *Physica D: Nonlinear Phenomena*, 67(1):257–281, 1993. [doi:10.1016/0167-2789\(93\)90210-R](https://doi.org/10.1016/0167-2789(93)90210-R).

[26] Z. Levnajić and I. Mezić. Ergodic theory and visualization. I. Mesochronic plots for visualization of ergodic partition and invariant sets. *Chaos: An Interdisciplinary Journal of Nonlinear Science*, 20(3):033114, 2010. [doi:10.1063/1.3458896](https://doi.org/10.1063/1.3458896).

[27] Z. Levnajić and I. Mezić. Ergodic theory and visualization. II. Fourier mesochronic plots visualize (quasi)periodic sets. *Chaos: An Interdisciplinary Journal of Nonlinear Science*, 25(5):053105, 2015. [doi:10.1063/1.4919767](https://doi.org/10.1063/1.4919767).

[28] C. Lopesino, F. Balibrea-Iniesta, V. J. García-Garrido, S. Wiggins, and A. M. Mancho. A theoretical framework for lagrangian descriptors. *International Journal of Bifurcation and Chaos*, 27:1730001, 2017. [doi:10.1142/S0218127417300014](https://doi.org/10.1142/S0218127417300014).

[29] C. Lopesino, F. Balibrea-Iniesta, V. J. García-Garrido, S. Wiggins, and A. M. Mancho. A theoretical framework for lagrangian descriptors. *International Journal of Bifurcation and Chaos*, 27(01):1730001, 2017. [arXiv:https://doi.org/10.1142/S0218127417300014](https://arxiv.org/abs/https://doi.org/10.1142/S0218127417300014), [doi:10.1142/S0218127417300014](https://arxiv.org/abs/https://doi.org/10.1142/S0218127417300014).

[30] C. Lopesino, F. Balibrea-Iniesta, S. Wiggins, and A. M. Mancho. Lagrangian descriptors for two dimensional, area preserving autonomous and nonautonomous maps. *Communications in Nonlinear Science and Numerical Simulation*, 27(1-3):40–51, 2015. [doi:10.1016/j.cnsns.2015.02.022](https://doi.org/10.1016/j.cnsns.2015.02.022).

[31] E. E. Macau and C. Grebogi. Control of chaos and its relevancy to spacecraft steering. *Philosophical Transactions of the Royal Society A: Mathematical, Physical and Engineering Sciences*, 364(1846):2463–2481, 2006.

[32] M. Macek and A. Levitan. Regularity and chaos at critical points of first-order quantum phase transitions. *Phys. Rev. C*, 84:041302, 2011. [doi:10.1103/PhysRevC.84.041302](https://doi.org/10.1103/PhysRevC.84.041302).

[33] J. A. J. Madrid and A. M. Mancho. Distinguished trajectories in time dependent vector fields. *Chaos*, 19:013111, 2009. [doi:10.1063/1.3056050](https://doi.org/10.1063/1.3056050).

[34] A. M. Mancho, S. Wiggins, J. Curbelo, and C. Mendoza. Lagrangian descriptors: a method for revealing phase space structures of general time dependent dynamical systems. *Communications in Nonlinear Science and Numerical Simulation*, 18(12):3530–3557, 2013. [doi:10.1016/j.cnsns.2013.05.002](https://doi.org/10.1016/j.cnsns.2013.05.002).

[35] B. Many Manda, M. Hillebrand, and C. Skokos. Efficient detection of chaos through the computation of the generalized alignment index (gali) by the multi-particle method. *Communications in Nonlinear Science and Numerical Simulation*, 143:108635, 2025. URL: <https://www.sciencedirect.com/science/article/pii/S1007570425000462>, [doi:10.1016/j.cnsns.2025.108635](https://doi.org/10.1016/j.cnsns.2025.108635).

[36] J. D. Meiss and E. Ott. Markov-tree model of intrinsic transport in hamiltonian systems. *Phys. Rev. Lett.*, 55:2741–2744, Dec 1985. URL: <https://link.aps.org/doi/10.1103/PhysRevLett.55.2741>, [doi:10.1103/PhysRevLett.55.2741](https://doi.org/10.1103/PhysRevLett.55.2741).

[37] C. Mendoza and A. M. Mancho. Hidden geometry of ocean flows. *Phys. Rev. Lett.*, 105:038501, 2010. [doi:10.1103/PhysRevLett.105.038501](https://doi.org/10.1103/PhysRevLett.105.038501).

[38] I. Mezić and S. Wiggins. A method for visualization of invariant sets of dynamical systems based on the ergodic partition. *Chaos: An Interdisciplinary Journal of Nonlinear Science*, 9(1):213–218, 03 1999. [arXiv:https://pubs.aip.org/aip/cha/article-pdf/9/1/213/18301537/213\\_1\\_online.pdf](https://arxiv.org/abs/https://pubs.aip.org/aip/cha/article-pdf/9/1/213/18301537/213_1_online.pdf), [doi:10.1063/1.166399](https://doi.org/10.1063/1.166399).

[39] M. Miguel Angel Bastarrachea-Magnani, L. del Carpio B., J. Chávez-Carlos, S. Lerma-Hernández, and J. Hirsch. Regularity and chaos in cavity QED. *Physica Scripta*, 92(5):054003, 2017. [doi:10.1088/1402-4896/aa6640](https://doi.org/10.1088/1402-4896/aa6640).

[40] H. Moges, T. Manos, O. Racoveanu, and C. Skokos. On the behavior of the Generalized Alignment Index (GALI) method for dissipative systems. *International Journal of Bifurcation and Chaos*, 35(09):2530021, 2025. [arXiv:https://doi.org/10.1142/S0218127425300216](https://arxiv.org/abs/https://doi.org/10.1142/S0218127425300216), [doi:10.1142/S0218127425300216](https://doi.org/10.1142/S0218127425300216).

[41] C. E. Montanari, R. B. Appleby, A. Bazzani, A. Fornara, M. Giovannozzi, S. Redaelli, G. Sterbini, and G. Turchetti. Chaos indicators for nonlinear dynamics in circular particle accelerators. *Eur. Phys. J. Plus*, 140(6):603, 2025. [arXiv:2504.12741](https://arxiv.org/abs/2504.12741), [doi:10.1140/epjp/s13360-025-06552-1](https://doi.org/10.1140/epjp/s13360-025-06552-1).

[42] J. Montes, F. Revuelta, and F. Borondo. Lagrangian descriptors and regular motion. *Communications in Nonlinear Science and Numerical Simulation*, 102:105860, 2021. URL: <https://www.sciencedirect.com/science/article/pii/S1007570421001726>, [doi:10.1016/j.cnsns.2021.105860](https://doi.org/10.1016/j.cnsns.2021.105860).

[43] S. Naik, V. J. García-Garrido, and S. Wiggins. Finding nhim: Identifying high dimensional phase space structures in reaction dynamics using lagrangian descriptors. *Communications in Nonlinear Science and Numerical Simulation*, 79:104907, 2019. URL: <https://www.sciencedirect.com/science/article/pii/S100757041930228X>, [doi:10.1016/j.cnsns.2019.104907](https://doi.org/10.1016/j.cnsns.2019.104907).

[44] A. V. Oppenheim, R. W. Schafer, and J. R. Buck. *Discrete-time signal processing (2nd ed.)*. Prentice-Hall, Inc., USA, 1999.

[45] Y. Papaphilippou. Detecting chaos in particle accelerators through the frequency map analysis method. *Chaos: An Interdisciplinary Journal of Nonlinear Science*, 24(2):024412, 06 2014. [arXiv:https://pubs.aip.org/aip/cha/article-pdf/doi/10.1063/1.4884495/19786722/024412\\\_1\online.pdf](https://arxiv.org/abs/https://pubs.aip.org/aip/cha/article-pdf/doi/10.1063/1.4884495/19786722/024412\_1\online.pdf), [doi:10.1063/1.4884495](https://doi.org/10.1063/1.4884495).

[46] P. Prince and J. Dormand. High order embedded runge-kutta formulae. *Journal of Computational and Applied Mathematics*, 7(1):67–75, 1981. URL: <https://www.sciencedirect.com/science/article/pii/0771050X81900103>, doi:10.1016/0771-050X(81)90010-3.

[47] Z. Sándor, B. Érdi, A. Széll, and B. Funk. The Relative Lyapunov Indicator: an efficient method of chaos detection. *Celestial Mechanics and Dynamical Astronomy*, 90(1):127–138, 2004. doi:10.1007/s10569-004-8129-4.

[48] H. Schuster and W. Just. *Deterministic Chaos: An Introduction*. Wiley, 2006. URL: <https://books.google.es/books?id=-14Y2WPfYgsC>.

[49] O. Semerák and P. Sukova. Free motion around black holes with discs or rings: between integrability and chaos - I. *Mon. Not. Roy. Astron. Soc.*, 404:545–574, 2010. arXiv: 1211.4106, doi:10.1111/j.1365-2966.2009.16003.x.

[50] I. I. Shevchenko. *Dynamical Chaos in Planetary Systems*, volume 463. 2020. doi: 10.1007/978-3-030-52144-8.

[51] C. Skokos. Alignment indices: a new, simple method for determining the ordered or chaotic nature of orbits. *Journal of Physics A: Mathematical and General*, 34(47):10029, 2001. doi:10.1088/0305-4470/34/47/309.

[52] C. Skokos. *The Lyapunov Characteristic Exponents and their computation*, pages 63–135. Lectures Notes in Physics, vol 790. Springer, Berlin, Heidelberg, 2010. doi: 10.1007/978-3-642-04458-8\_2.

[53] C. Skokos, C. Antonopoulos, T. Bountis, and M. Vrahatis. How does the Smaller Alignment Index (SALI) distinguish order from chaos? *Progress of Theoretical Physics Supplement*, 150:439–443, 2003. doi:10.1143/PTPS.150.439.

[54] C. Skokos, C. Antonopoulos, T. Bountis, and M. Vrahatis. Detecting order and chaos in Hamiltonian systems by the SALI method. *Journal of Physics A: Mathematical and General*, 37(24):6269, 2004. doi:10.1088/0305-4470/37/24/006.

[55] C. Skokos, T. Bountis, and C. Antonopoulos. Geometrical properties of local dynamics in Hamiltonian systems: the Generalized Alignment Index (GALI) method. *Physica D: Nonlinear Phenomena*, 231(1):30–54, 2007. doi:10.1016/j.physd.2007.04.004.

[56] C. Skokos, G. Gottwald, and J. Laskar. *Chaos detection and predictability*. Lecture Notes in Physics. Springer Berlin Heidelberg, 2016. doi:10.1007/978-3-662-48410-4.

[57] J. Sonnenschein and N. Shrayer. On chaos in QFT, 2025. URL: <https://arxiv.org/abs/2506.10784>, arXiv:2506.10784.

[58] Y. Susuki and I. Mezić. Ergodic partition of phase space in continuous dynamical systems. In *Proceedings of the 48h IEEE Conference on Decision and Control (CDC) held jointly with 2009 28th Chinese Control Conference*, pages 7497–7502, 2009. doi: 10.1109/CDC.2009.5400911.

[59] S. Suzuki and K.-i. Maeda. Chaos in schwarzschild spacetime: The motion of a spinning particle. *Phys. Rev. D*, 55:4848–4859, Apr 1997. URL: <https://link.aps.org/doi/10.1103/PhysRevD.55.4848>, doi:10.1103/PhysRevD.55.4848.

[60] M. Takahashi and H. Koyama. Chaotic motion of Charged Particles in an Electromagnetic Field Surrounding a Rotating Black Hole. *Astrophys. J.*, 693:472–485, 2009. arXiv:0807.0277, doi:10.1088/0004-637X/693/1/472.

[61] A. A. Tsonis and J. B. Elsner. Chaos, strange attractors, and weather. *Bulletin of the American Meteorological Society*, 70(1):14 – 23, 1989. URL: [https://journals.ametsoc.org/view/journals/bams/70/1/1520-0477\\_1989\\_070\\_0014\\_csaaw\\_2\\_0\\_co\\_2.xml](https://journals.ametsoc.org/view/journals/bams/70/1/1520-0477_1989_070_0014_csaaw_2_0_co_2.xml), doi:10.1175/1520-0477(1989)070<0014:CSAAW>2.0.CO;2.

[62] P. Virtanen et al. SciPy 1.0—Fundamental algorithms for scientific computing in Python. *Nature Meth.*, 17:261, 2020. arXiv:1907.10121, doi:10.1038/s41592-019-0686-2.

- [63] P. Welch. The use of fast fourier transform for the estimation of power spectra: A method based on time averaging over short, modified periodograms. *IEEE Transactions on Audio and Electroacoustics*, 15(2):70–73, 1967. [doi:10.1109/TAU.1967.1161901](https://doi.org/10.1109/TAU.1967.1161901).
- [64] S. Wiggins and V. J. García-Garrido. Painting the phase portrait of a dynamical system with the computational tool of Lagrangian descriptors. *Notices of the American Mathematical Society*, 69(6):936–949, 2022. [doi:10.1090/NOTI2489](https://doi.org/10.1090/NOTI2489).
- [65] S. Wiggins, V. J. García-Garrido, and M. Katsanikas. *Phase Space Structures in Reaction Dynamics*. WORLD SCIENTIFIC, 2025. [doi:10.1142/14372](https://doi.org/10.1142/14372).
- [66] S. Zimper, A. Ngapasare, M. Hillebrand, M. Katsanikas, S. Wiggins, and C. Skokos. Performance of chaos diagnostics based on lagrangian descriptors. application to the 4d standard map. *Physica D: Nonlinear Phenomena*, 453:133833, 2023. [doi:10.1016/j.physd.2023.133833](https://doi.org/10.1016/j.physd.2023.133833).
- [67] E. E. Zotos. Distinguishing between order and chaos in a simple barred galaxy model. *Astronomische Nachrichten*, 338(5):614–620, 2017. [doi:10.1002/asna.201713152](https://doi.org/10.1002/asna.201713152).